A&A, 689, A42 (2024)
https://doi.org/10.1051/0004-6361/202449528

Astronomy & Astrophysics

Improved model of the Supernova Refsdal cluster MACS J1149.5+2223 thanks to *VLT*/MUSE⋆

S. Schuldt[1,2,⋆⋆], C. Grillo[1,2], G. B. Caminha[3,4], A. Mercurio[5,6,7], P. Rosati[8,9], T. Morishita[10], M. Stiavelli[11], S. H. Suyu[3,4,12], P. Bergamini[1,9], M. Brescia[13], F. Calura[9], and M. Meneghetti[9]

[1] Dipartimento di Fisica, Università degli Studi di Milano, via Celoria 16, 20133, Milano, Italy
[2] INAF – IASF Milano, via A. Corti 12, 20133 Milano, Italy
[3] Technical University of Munich, TUM School of Natural Sciences, Department of Physics, James-Franck-Straße 1, 85748 Garching, Germany
[4] Max-Planck-Institut für Astrophysik, Karl-Schwarzschild Straße 1, 85748 Garching, Germany
[5] Università di Salerno, Dipartimento di Fisica "E.R. Caianiello", Via Giovanni Paolo II 132, 84084 Fisciano (SA), Italy
[6] INAF – Osservatorio Astronomico di Capodimonte, Via Moiariello 16, 80131 Napoli, Italy
[7] INFN – Gruppo Collegato di Salerno – Sezione di Napoli, Dipartimento di Fisica "E.R. Caianiello", Università di Salerno, via Giovanni Paolo II 132, 84084 Fisciano (SA), Italy
[8] Dipartimento di Fisica e Scienze della Terra, Università degli Studi di Ferrara, via Saragat 1, 44122 Ferrara, Italy
[9] INAF – OAS, Osservatorio di Astrofisica e Scienza dello Spazio di Bologna, via Gobetti 93/3, 40129 Bologna, Italy
[10] IPAC, California Institute of Technology, MC 314-6, 1200 E. California Boulevard, Pasadena, CA 91125, USA
[11] Space Telescope Science Institute, 3700 San Martin Drive, Baltimore, MD 21218, USA
[12] Academia Sinica Institute of Astronomy and Astrophysics (ASIAA), 11F of ASMAB, No.1, Section 4, Roosevelt Road, Taipei 10617, Taiwan
[13] Dipartimento di Fisica "E. Pancini", Università degli Studi di Napoli Federico II, Via Cinthia, 21, 80126 Napoli, Italy

Received 7 February 2024 / Accepted 17 May 2024

ABSTRACT

We present new VLT/MUSE observations of the *Hubble* Frontier Field (HFF) galaxy cluster MACS J1149.5+2223, lensing the well-known supernova "Refsdal" into multiple images, which has enabled the first cosmological applications with a strongly lensed supernova. Thanks to these data, targeting a northern region of the cluster and thus complementing our previous MUSE program on the cluster core, we have released a new catalog containing 162 secure spectroscopic redshifts. We confirmed 22 cluster members, which had previously been only photometrically selected, and detected ten additional ones, resulting in a total of 308 secure members, of which 63% are spectroscopically confirmed. We further identified 17 new spectroscopic multiple images belonging to six different background sources. By exploiting these new and our previously published MUSE data, in combination with the deep HFF images, we developed an improved total mass model of MACS J1149.5+2223. This model includes 308 total mass components for the member galaxies and requires four additional mass profiles, one of which is associated with a cluster galaxy overdensity identified in the north, representing the dark matter mass distribution on larger scales. The values of the resulting 34 free parameters are optimized based on the observed positions of 106 multiple images from 34 different families, that cover an extended redshift range between 1.240 and 5.983. Our final model has a multiple image position root mean square value of 0.39″, which is in good agreement with other cluster lens models based on a similar number of multiple images. With this refined mass model, we have paved the way toward an improved strong-lensing analyses that will exploit the deep and high resolution observations with HST and JWST on a pixel level in the region of the supernova Refsdal host. This will increase the number of observables by around two orders of magnitude, thus offering the opportunity to carry out more precise and accurate cosmographic measurements in the future.

Key words. gravitational lensing: strong – methods: data analysis – catalogs – galaxies: clusters: general – galaxies: distances and redshifts – galaxies: clusters: individual: MACS J1149.5+2223

1. Introduction

Gravitational lensing describes the effect of a massive object, such as a galaxy cluster, deflecting the light coming from background sources. It enables us to probe several different aspects of the Universe. Since the deflection depends on the total mass of a lens, that is, both the dark matter and baryonic components, gravitational lensing can be used to study its dark matter mass distribution (e.g., Grillo et al. 2015; Limousin et al. 2016; Cerny et al. 2018; Schuldt et al. 2019; Meneghetti et al. 2020, 2022, 2023; Shajib et al. 2021; Wang et al. 2022). Furthermore, it allows the study of the evolution of galaxy clusters (e.g., Annunziatella et al. 2016; Mercurio et al. 2021) and faint high-redshift galaxies that are observable thanks to the lensing magnification effect (e.g., Coe et al. 2013; Calura et al. 2021; Vanzella et al. 2021; Meštrić et al. 2022).

In addition, in the rare case of a multiply imaged time-variable source, such as a quasar or a supernova (SN), lensing gives us a unique opportunity to exploit these lensing systems for cosmological applications, including the measurement of the Hubble constant H_0 and of the geometry of the Universe (see Treu et al. 2022;

⋆ This work is based in large part on data collected at ESO VLT (prog.IDs 294.A-5032 and 105.20P5.001) and NASA HST.
⋆⋆ Corresponding author; stefan.schuldt@unimi.it

Suyu et al. 2024, and references therein). This technique is called time-delay cosmography. To date, SN "Refsdal" ($z = 1.489$, Kelly et al. 2015a; Kelly 2016) is the only strongly lensed supernova used for precise time-delay cosmography (e.g., Grillo et al. 2018, 2020, 2024; Kelly et al. 2023), making the lens cluster a unique and well studied field. Given the increasing number of detected SNe strongly lensed by galaxy clusters (e.g., Kelly et al. 2015b; Rodney et al. 2016, 2021; Frye et al. 2024; Pierel et al. 2024), where the time delays are on the order of months to years, compared to those of days to weeks of galaxy-scale systems, detailed total mass models of these lens clusters will become crucial for time-delay cosmography.

SN Refsdal is multiply imaged by the *Hubble* Frontier Field (HFF) galaxy cluster MACS J1149.5+2223 (hereafter, MACS 1149; Treu et al. 2016; Grillo et al. 2016, hereafter G16) located at a redshift of $z_c = 0.5422$. Given that it is in the HFF cluster sample, as well as being part of the Cluster Lensing And Supernova survey with *Hubble* (CLASH, Postman et al. 2012) and the Grism Lens-Amplified Survey from Space (GLASS, Treu & Ellis 2015; Schmidt et al. 2014), this cluster is equipped with extensive spectroscopic and photometric data. This set of data is complemented by deep Multi Unit Spectroscopic Explorer (MUSE, Bacon et al. 2012) observations of the cluster core carried out by G16 to securely select cluster members and multiple image systems for a robust strong lensing model (see Fig. 1).

To further expand the data set of this peculiar lens cluster and to improve on the strong lensing model, we present additional 5.5 hours of MUSE observations (PI A. Mercurio) from the Very Large Telescope (VLT) of the European Southern Observatory. These observations were carried out in 2022 and 2023, and targeted a region in the northern part of the cluster (see Fig. 2). Therefore, these observations perfectly complement our previous MUSE data, enabling us to significantly extend our redshift catalog with new spectroscopic redshifts. They also reveal several new multiply lensed sources and spectroscopically confirms numerous cluster members, that had previously only been photometrically identified.

By exploiting these new MUSE observations, complemented with existing high-quality spectroscopic and photometric data, we present an improved total mass model of the cluster MACS 1149. We incorporated all newly identified multiple images and take all 308 securely identified cluster members into account. We herewith publicly release the presented cluster lens model, which is poised to play a fundamental role in improving time-delay cosmography and in studying the intrinsic properties of high-redshift sources (see, e.g., Stiavelli et al. 2023; Morishita et al. 2024a,b).

The paper is organized as follows. We introduce the HST data in Sect. 2, and the spectroscopic data obtained with MUSE in Sect. 3, along with the latest redshift catalog of MACS 1149 and a discussion of the newly discovered multiply imaged sources. In Sect. 4, we describe our strong lensing mass model of the cluster and the tested mass parametrizations. The results and conclusions are given in Sect. 5.

Throughout this paper, we assume a flat ΛCDM cosmology with $H_0 = 70\,\mathrm{km\,s^{-1}\,Mpc^{-1}}$ and $\Omega_M = 1 - \Omega_{DE} = 0.3$. In this cosmology, $1''$ corresponds to 6.36 kpc at the cluster redshift $z_c = 0.5422$. All magnitudes are given in the AB system (Oke & Gunn 1983; Fukugita et al. 1996).

2. HST imaging

The cluster MACS 1149 was observed as part of the CLASH (PI M. Postman) and HFF (PI J. Lotz) programs with more than 50 HST orbits in 15 broadband filters. These data, complemented with previously obtained images (see Postman et al. 2012; Zheng et al. 2012; Jouvel et al. 2014), were processed with standard calibration techniques and drizzled to mosaics (see e.g., Koekemoer et al. 2007, 2011). In this work, we use all available filters of the HFF stacks with a pixel size of $0.03''$, shown in Fig. 1, to confirm multiple image systems (see Sect. 3.2.2) and the HFF $F160W$ image for the cluster member selection (see Sect. 3.2.1).

3. VLT/MUSE spectroscopy

MACS 1149 was observed with the VLT/MUSE instrument in two campaigns. The first data set was obtained in 2015 under the ESO programme ID 294.A-5032 (PI C. Grillo) and covered the core of the cluster, including the SN Refsdal host galaxy, for a total exposure time of 4.8 hours. As stated in G16, the observational conditions were clear and photometric with a seeing of $0.81''$.

Additional 5.5 hours of MUSE observations, centered on the north-west region of the cluster (see Fig. 1), were obtained in 2022 and 2023 under the programme ID 105.20P5 (PI A. Mercurio). The data were taken in clear sky and good seeing ($0.76''$) conditions. In the following, we present the data reduction procedure and resulting redshift catalog.

3.1. Data reduction

As described in G16, the MUSE observations from 2015 were reduced with the MUSE data reduction software version 1.0 in 2015. Given the small overlap between this MUSE pointing and the new observations taken in 2022 and 2023 (see Fig. 1), we performed a new, combined data reduction with the pipeline version 2.8.5. We followed the standard procedure, such as bias subtraction, flat-fielding, wavelength calibration, and exposure map alignment. We refer to G16 and Karman et al. (2016) for further details.

The MUSE datacube was aligned with the HST images, using as references the HST $F606W$ band and the MUSE "white image". We degraded the HST image to the MUSE white image resolution and employed the positions of 94 compact sources to match both data sets. The root mean square (RMS) separation of the final matched data sets is $0.054''$, thus significantly below the MUSE pixel size of $0.2''$. Furthermore, we found no evidence of relative rotation between MUSE and HST.

3.2. Spectral analysis

Since the MUSE observations from 2015 were already analyzed, only each extracted spectrum from the new MUSE data, including a re-inspection of objects in the area covered by both MUSE pointings, was inspected individually. As already done in previous MUSE redshift catalogs, we assign to each redshift value a quality flag (QF) that indicates its reliability. A QF of 3 corresponds to a very secure ($\delta z < 0.001$) measurement, while a QF of 2 corresponds to a secure ($\delta z < 0.01$) one, and of 1 to an unsecure ($\delta z \geq 0.01$) one. A QF of 9 is provided for redshifts that are based on a single emission line, and, since the MUSE spectral resolution allows us to distinguish the shape or doublet nature of narrow emission lines (e.g., Lyman-α and O_{II}), considered as secure. These error estimates include systematic uncertainties due to different methods of redshift measurements. Following these criteria, we have 162 secure (i.e., QF > 1)

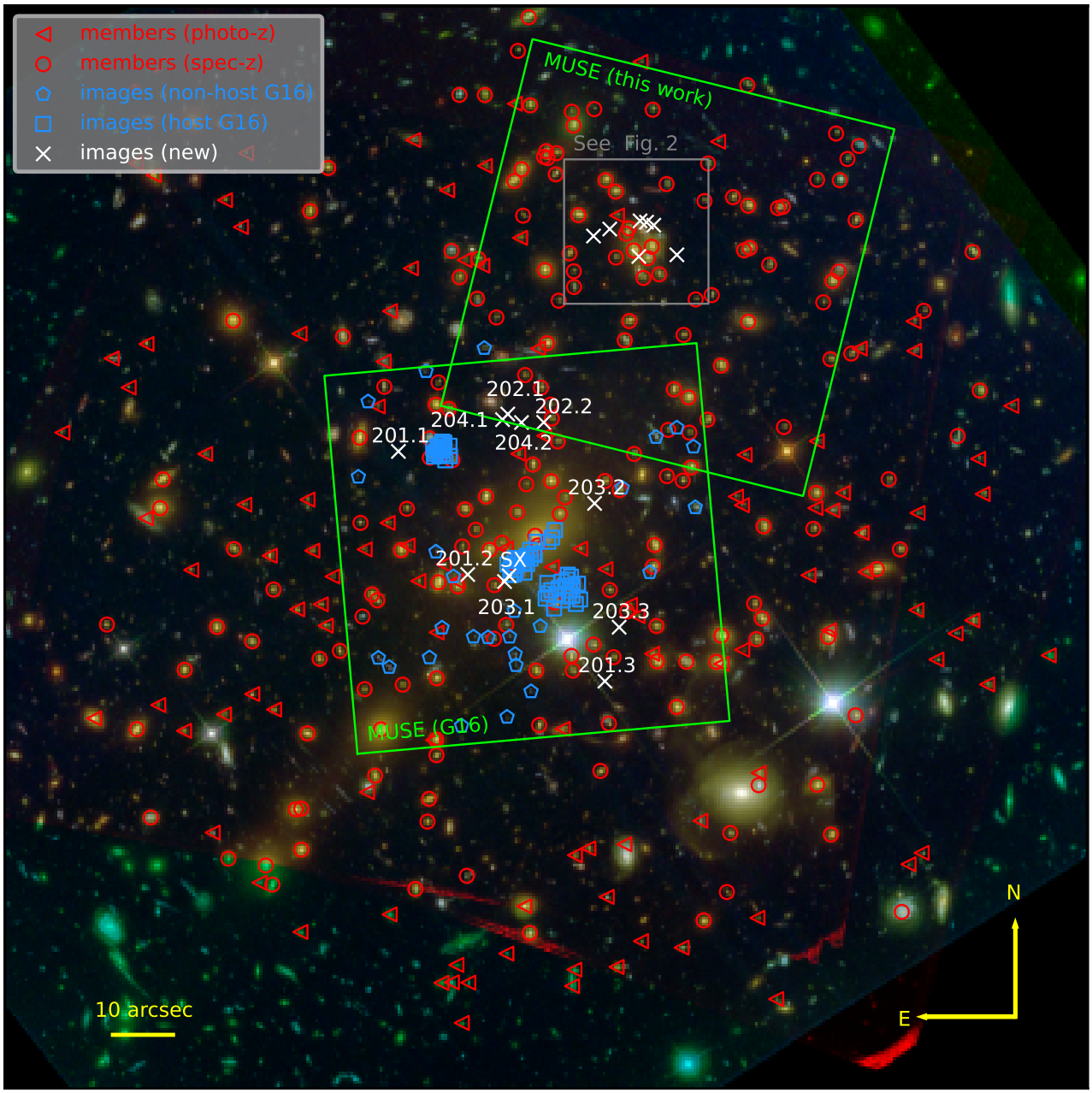

Fig. 1. Color-composite image of MACS 1149 obtained by combining the HFF observations ($F435W + F465W$ for blue, $F555W + F606W + F625W + F775W + F814W + F850LP$ for green, and $F105W + F110W + F125W + F140W + F160W$ for red). The cluster members (red) either photometrically selected (triangle) or spectroscopically confirmed (circle), and the multiple image systems are shown. We distinguish the multiple images between those previously known from G16 (blue), either belonging to the SN Refsdal host (square) or at other redshifts (pentagon), and those newly identified in this work (white). We highlight the regions observed with MUSE (green) and the zoom-in region (gray) shown in Fig. 2.

redshifts, which we list in Table A.1. Given the redshift uncertainty, the spectral resolution of MUSE, and the number of identified lines in the spectra, we follow our previous publications and provide redshift values with four digits after the decimal point for foreground objects and cluster members, but with three digits for background sources.

The secure redshifts listed in Table A.1 are integrated in the previous redshift catalog from G16, which contains now 509 spectroscopic redshifts and is made available in electronic form with this publication[1]. We show a histogram of the full redshift catalog in Fig. 3, divided into redshifts previously published by G16 (gray) and new redshifts (blue). This highlights the significant increase in the covered redshift range, as we have now several secure redshifts up to $z \sim 6$.

3.2.1. Cluster members

To select the cluster members of MACS 1149, we adopted the same selection criteria as in G16. In short, we selected all galaxies that have a secure redshift in the range $0.520 \leq z \leq 0.570$, which are either spectroscopically confirmed with MUSE (G16, and this work) or obtained from GLASS (Treu et al. 2016).

[1] We release the redshift catalog at the following link upon publication: https://www.fe.infn.it/astro/lensing/

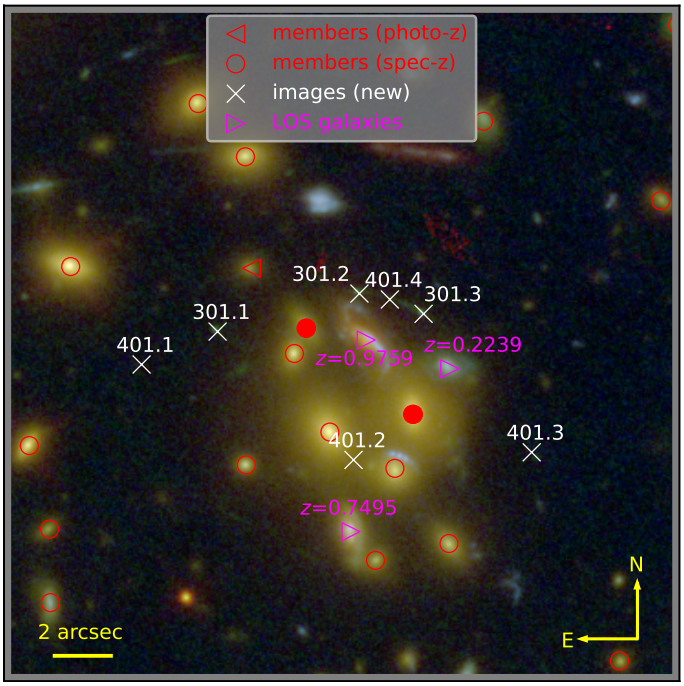

Fig. 2. Color-composite image (as in Fig. 1) of the galaxy group in the northern field of MACS 1149. Shown are the cluster members (red) and the multiple image systems (white). Furthermore, we indicate three line-of-sight galaxies (magenta), with the corresponding redshift values, and two cluster members (red-filled circles) whose effect on the total lens mass model was tested (see Sect. 4.4 for more details).

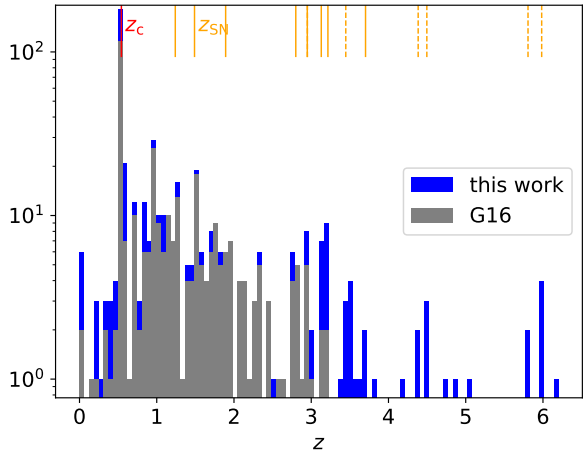

Fig. 3. Stacked histogram of the redshift distribution in the MACS 1149 field, divided into previously known (gray, G16) and new or updated[2] (blue) redshifts. As a reference, the redshift of the cluster $z_c = 0.5422$ is indicated by a red line and that of multiply lensed sources with orange lines (solid and dashed lines for the previously known and new identifications, respectively), including SN Refsdal at $z_{SN} = 1.489$.

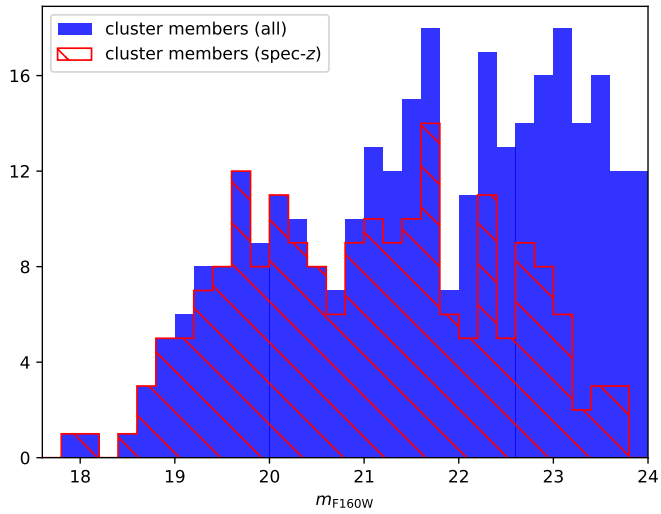

Fig. 4. Histogram of the cluster member magnitudes in the HFF $F160W$ band.

These spectroscopically confirmed cluster members are, where possible, centered on their luminosity centroids on the HFF images; otherwise the coordinates of the spectroscopic detection itself are used. This spectroscopic sample is complemented with robust photometrically selected members as in G16.

Since the total mass of a cluster member is assumed to scale according to the galaxy total luminosity in the $F160W$ band (see Sect. 4.2), we included in the cluster total mass model only the most massive cluster members, namely, those that are brighter than $m_{F160W} = 24$, as done in G16. This frequently adopted limit is well below the threshold of $m_{F160W} \leq 21$, identified by Bergamini et al. (2023), after which no significant difference in the accuracy of a cluster total mass reconstruction was observed. This is also in agreement with Raney et al. (2021), who have tested the same threshold in the $F814W$ band. To measure the galaxy $F160W$ total magnitudes, we adopted Kron magnitudes, which approximate those extracted from GALFIT (Peng et al. 2002) very well (G16), resulting in reliable and unbiased total magnitudes. For this purpose, we favored the image from the HFF program over the shallower CLASH image used in G16. As a consequence, we obtained slightly different magnitudes and excluded now one cluster member (ID 143 in Table 6 of G16) as it was fainter than $m_{F160W} = 24$. In contrast, we included six new members, in the outer regions of the cluster, which fall now inside the HST FoV. The distribution of the cluster member magnitudes is shown in Fig. 4.

Thanks to the new MUSE observations, we were able to spectroscopically confirm 22 cluster members that were previously only photometrically selected. Furthermore, we rejected one cluster member, making it to a photometric outlier (member ID 46 in Table 6 of G16), while four objects (member IDs 305, 306, 308, 309) that were previously excluded from the member sample, based on the spectroscopic redshifts from GLASS, are now included among the cluster members. These four members are relatively faint ($m_{F160W} > 22.6$), possibly explaining the wrong measurement in Treu et al. (2016). Given their low total luminosity, we expect that excluding them in previously presented cluster mass models would affect them only slightly.

In summary, we were able to securely identify 308 cluster members, containing in total 195 spectroscopically confirmed members (i.e., 63.3%); of these, ten were entirely new members. The members are listed in Table 1 and shown in Fig. 1 (in red). The parametrization of the cluster members in the total mass model and the impact of the changes compared to G16 are presented in Sect. 4.

[2] For example, the redshift of the multiple images 13261 and 13457 at $z = 3.704$ (listed as family 14 in Table 2 of G16).

Table 1. Cluster members of MACS 1149 considered in our mass model.

ID	RA (J2000)	Dec (J2000)	$F160W$ [mag]	Sel. criterion
1	177.37311	22.39300	21.17 ± 0.01	P
2	177.37497	22.40452	23.26 ± 0.03	P
3	177.37618	22.39166	22.24 ± 0.01	P
4	177.37640	22.40045	22.26 ± 0.02	P
5	177.37655	22.40522	20.41 ± 0.05	G
6	177.37663	22.40207	23.30 ± 0.04	P
7	177.37692	22.39462	21.20 ± 0.01	P
8	177.37766	22.40312	21.18 ± 0.07	G
9	177.37776	22.39401	23.75 ± 0.03	P
10	177.37871	22.39281	22.77 ± 0.02	P
⋮	⋮	⋮	⋮	⋮

Notes. Columns give, from left to right, the IDs following Table 6 of G16, right ascension, declination, and the magnitude from the HFF $F160W$ image with the corresponding uncertainty. In the last column, we indicate whether it was selected photometrically (P), based on the WFC3-IR-GRISM redshift (G) from GLASS (Treu et al. 2016), the MUSE observations presented in G16 (M1), or in this publication (M2). This catalog is downloadable in its entirety from the web[3].

3.2.2. Multiply lensed sources

Based on the newly obtained MUSE redshifts (see Table A.1), we identified two sources that are multiply lensed by the galaxy group located in the northern region of MACS 1149 (see Fig. 2). One source (ID 301), lying at $z = 3.447$, is triply lensed, and visible in the HST images, while the other (ID 401), at $z = 5.983$, is quadruply lensed and only detected in the MUSE data. We show the corresponding spectra in Fig. 5. We further observe two sources (IDs 202 and 204), which are both doubly lensed. The first one is at $z = 4.384$ and detected by HST, while the other one, at $z = 5.806$, was only identified through a single emission line in the MUSE spectra (see Fig. 5).

We carried out a dedicated search for simultaneously appearing spectral features when scanning the old and new, combined MUSE data cube to detect possible multiple images. With this procedure, which joins an automatic detection and a visual inspection (see Sect. 2.2 of Caminha et al. 2023), we found two multiply lensed sources (ID 201 and 203) that were previously unknown. Both are observed three times and, again, one (ID 203) of the two has only been detected by MUSE. We show their spectra in Fig. 5 as well.

We summarize all the newly identified multiple images in Table 2, which are also marked in Fig. 1 (white cross). They are included in our lensing model presented in Sect. 4, complemented by those published by G16 and the fifth image SX of SN Refsdal, published by Kelly et al.(2016, marked in white in Fig. 1).

4. Lens modeling

The strong lensing analysis follows closely that presented in G16, so we refer to that work, as well as to Grillo et al. (2015), for a detailed discussion of the modeling and statistical analysis. In the following, we summarize the procedure and highlight the differences compared to the previous model from G16.

[3] https://www.fe.infn.it/astro/lensing/

The cluster total mass model was obtained with the Gravitational Lens Efficient Explorer (GLEE, Suyu & Halkola 2010; Suyu et al. 2012) software. This software has been widely used for strong-lens modeling, in particular for time-delay cosmography on galaxy-scale (e.g., Wong et al. 2020; Ertl et al. 2023; Shajib et al. 2022) as well as on cluster-scale (Grillo et al. 2018, 2020, 2024) systems. The software supports mainly simply parameterized and physically motivated mass density profiles, as introduced below, to describe the total mass distribution of a lens. It provides several optimization and Bayesian sampling algorithms to infer the best-fitting parameter values and to sample their parameter space. Here, we preferentially relied on the simulated annealing, the Markov chain Monte Carlo (MCMC) technique, and its parallelized version `emcee` (Foreman-Mackey et al. 2013), with the main advantage of decreasing the computational time. We further used and extended *glee_tool.py* (Schuldt et al. 2023), a code that supports several tools for modeling with GLEE and helps to reduce the user input time.

In the following, we detail the adopted mass density profiles, how we include the multiple images as constraints, and which model configurations we consider. Finally, we give a summary of our final model and the corresponding results.

4.1. Multiple image systems

The total mass distribution of MACS 1149 is reconstructed from securely identified multiply lensed sources. We include 62 multiple images that belong to 18 different knots of the SN Refsdal host galaxy (see Table 3 of G16), and 26 multiple images from ten different sources (see Table 2 in G16). Moreover, we now added the fifth image of SN Refsdal (referenced as SX), which has been detected in December 2015 (Kelly et al. 2015a, 2016). These previously known systems have now been complemented thanks to our recent MUSE observations (see Sect. 3), with 17 new multiple images from six different sources, listed in Table 2. The combination resulted in a total of 106 multiple images from 34 different families covering a redshift range between 1.24 and 5.98, with most constraints at $z_{\rm SN} = 1.489$ from SN Refsdal and its host. The redshifts of all multiply lensed sources are highlighted with orange lines in Fig. 3.

While 31 families are spectroscopically confirmed, three are photometrically identified systems from the "gold" sample presented in Table 3 of Treu et al. (2016). As in previous strong lensing models, these last systems are included with a redshift value free to vary. We adopted for them a broad range between zero and six, with a flat prior. This leads to three free parameters, in addition to their variable source positions ($34 \times 2 = 68$ free parameters), beside the mass model free parameters (see Sect. 4.2 and Sect. 4.3 for more details), while providing ($106 \times 2 =$) 212 positional constraints for the model.

4.2. Cluster member mass component

We included in our total mass model all the 308 cluster members identified in Sect. 3.2.1 with the same total mass density profile. These mass components are centered on the galaxy luminosity centroid positions (see Table 1) and described by a dual pseudo-isothermal elliptical mass distribution (dPIE; Elíasdóttir et al. 2007; Suyu & Halkola 2010) with axis ratio $q \equiv 1$ and vanishing core radius, such that the convergence (or dimensionless surface mass density) κ of the cluster member j can be expressed as

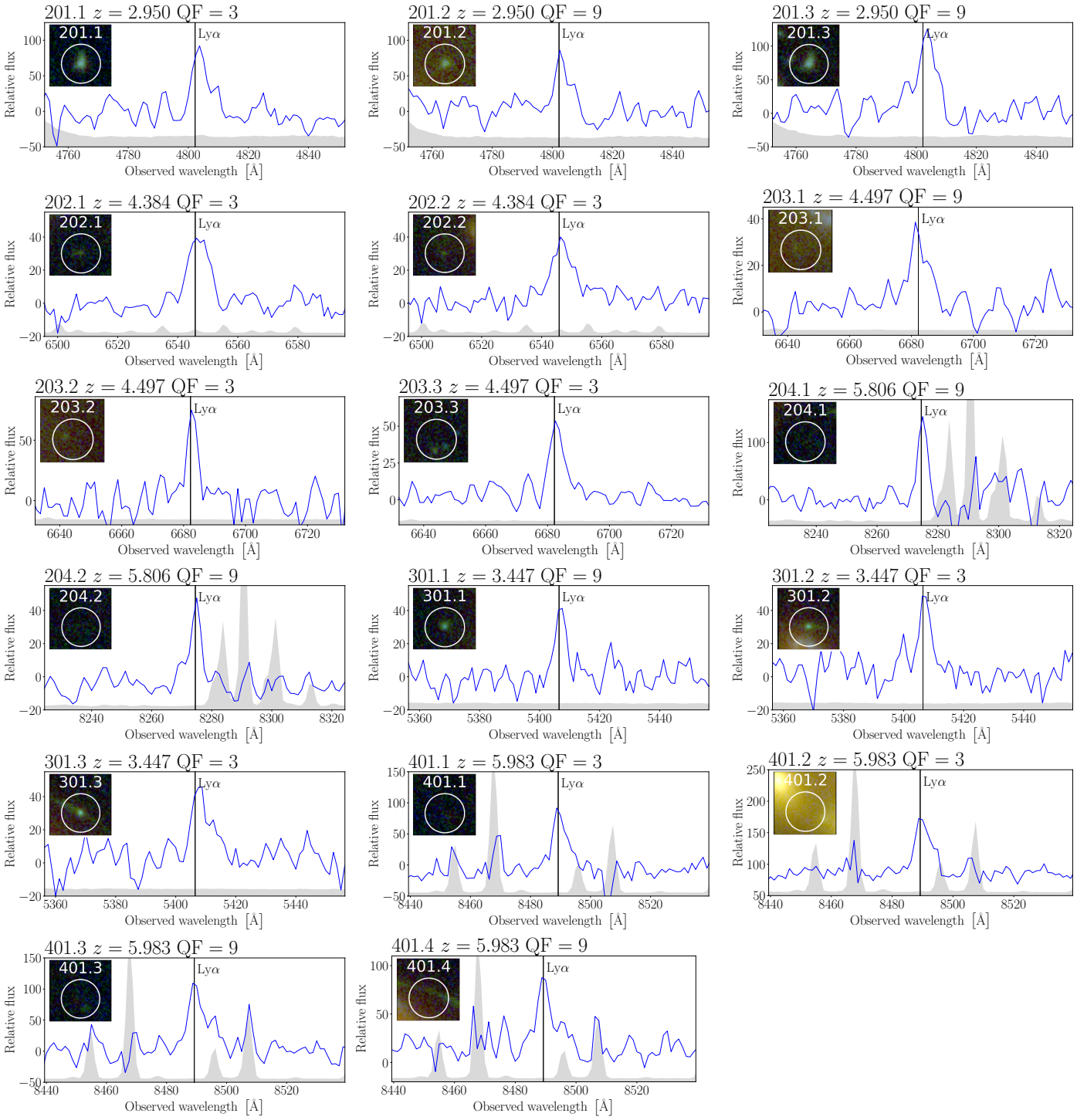

Fig. 5. Spectra of the newly discovered multiple images. The vertical line indicates the observed position of the Lyman-α emission and the rescaled variance is shown in gray. ID, redshift and quality flag are indicated in each figure title. The HST cutouts are 2″ on each side, and north is up and east is left.

$$\kappa_j(x,y) = \frac{\theta_{\mathrm{E},j}}{2}\left(\frac{1}{\sqrt{x^2+y^2}} - \frac{1}{\sqrt{x^2+y^2+r_{\mathrm{t},j}^2}}\right). \quad (1)$$

The values of the Einstein radius $\theta_{\mathrm{E},j}$ and of the truncation radius $r_{\mathrm{t},j}$ are connected to those of the brightest cluster galaxy (BCG, ID 166 in Table 1) through their measured total luminosity L_j or magnitudes m_j (HST $F160W$ band, see Table 1) following the scaling relations

$$\theta_{\mathrm{E},j} = \theta_{\mathrm{E,BCG}}\left(\frac{L_j}{L_{\mathrm{BCG}}}\right)^{0.7} = \theta_{\mathrm{E,BCG}} \times 10^{0.28(m_{\mathrm{BCG}}-m_j)} \quad (2)$$

and

$$r_{\mathrm{t},j} = r_{\mathrm{t,BCG}}\left(\frac{L_j}{L_{\mathrm{BCG}}}\right)^{0.5} = r_{\mathrm{t,BCG}} \times 10^{0.2(m_{\mathrm{BCG}}-m_j)}, \quad (3)$$

Table 2. New multiple images, in addition to those from Tables 2 and 3 of G16, used in our strong lensing model of MACS 1149.

ID	RA (J2000)	Dec (J2000)	z_{sp}	QF	identification
SX [(a)]	177.40021	22.39681	1.489	3	HST
201.1	177.40562	22.40243	2.950	3	HST
201.2	177.40216	22.39675	2.950	9	HST
201.3	177.39530	22.39182	2.950	9	HST
202.1	177.40014	22.40415	4.384	3	HST
202.2	177.39834	22.40378	4.384	3	HST
203.1	177.40028	22.39641	4.497	9	MUSE
203.2	177.39575	22.40000	4.497	3	MUSE
203.3	177.39457	22.39442	4.497	3	MUSE
204.1	177.40043	22.40389	5.806	9	MUSE
204.2	177.39949	22.40376	5.806	9	MUSE
301.1	177.39504	22.41269	3.447	9	HST
301.2	177.39353	22.41307	3.447	3	HST
301.3	177.39285	22.41287	3.447	3	HST
401.1	177.39591	22.41239	5.983	3	MUSE
401.2	177.39357	22.41142	5.983	3	MUSE
401.3	177.39168	22.41153	5.983	9	MUSE
401.4	177.39319	22.41295	5.983	9	MUSE

Notes. Columns give, from left to right, the identification number ID, right ascension, declination, spectroscopic redshift z_{sp}, the corresponding redshift uncertainty in terms of a quality flag QF, and whether the image position is measured in the HST images or only from the MUSE data cube. Considered quality flags are: 3 very secure ($\delta z < 0.001$) and 9 secure (based on a single emission line). [(a)]Published in Kelly et al. (2016).

respectively. This means that we are able to effectively vary only two parameters to determine the total mass distribution of all cluster members, namely the Einstein radius $\theta_{E,BCG}$, and the truncation radius $r_{t,BCG}$ of the BCG.

Since the region around SN Refsdal is particularly interesting for cosmological applications (see e.g., Grillo et al. 2020, 2024) and very well constrained through 62 multiple images, associated with 18 knots of the SN host galaxy (see Sect. 3.2.2 and Table 3 in G16), we treated two galaxy members separately. These two members are located close the images of SN Refsdal, and we allowed, as done in G16, their dPIE profiles to have the Einstein and truncation radii free to vary outside of the scaling relations defined above. We further introduced an ellipticity term. This added up to eight additional free parameters, which is a small number, given the high number of observables in that region, and which are necessary to reconstruct the Fermat potential around the multiple images of SN Refsdal properly.

4.3. Cluster-scale mass components

In addition to including a total mass component for each cluster member, we also modeled the cluster mass distribution on larger scales. This is mainly the dark matter (DM) of the cluster halos not associated with the individual galaxies, such that we refer to them as DM halos in the following. This mass term is described by multiple pseudo-isothermal elliptical mass distributions (PIEMDs; Kassiola & Kovner 1993) characterized by six parameters: the coordinates of the center x_H and y_H; the axis ratio q_H; its orientation ϕ_H; the halo strength (or Einstein radius) $\theta_{E,H}$; and the core radius $r_{c,H}$.

Because of the complex merging state of MACS 1149, as revealed by Chandra X-ray observations (see Ogrean et al. 2016; Golovich et al. 2016), we followed the results of previous strong-lensing analyses (e.g., Smith et al. 2009; Rau et al. 2014; Grillo et al. 2016) and included in the initial cluster total mass model three PIEMD profiles. This results in 18 free parameters for the cluster-scale components.

4.4. Mass models

We started with the parametrization of G16, as described above, which means we include 308 dPIE profiles for the cluster members and three DM halos. By incorporating the new multiple images listed in Table 2 and adopting the usual χ^2 definition, the model cannot reproduce the correct image multiplicity of some families. This holds particularly for the two families around the galaxy group in the north (IDs 301 and 401, see Fig. 2). This might be due to an oversimplified parametrization of the total lens mass distribution, as we included only the mass of the cluster members through the scaling relations, while fully neglecting background and foreground galaxies and the specific DM halo associated with this group.

To avoid models with wrong image multiplicity, we modify the usual χ^2 definition in the following way

$$\chi^2 = \sum_{j=1}^{N^{\rm fam}} \begin{cases} \sum_{k=1}^{N_j^{\rm obs}} \frac{\left(x_{j,k}^{\rm obs} - x_{j,k}^{\rm pred}\right)^2}{\Delta x_{j,k}^2} + \frac{\left(y_{j,k}^{\rm obs} - y_{j,k}^{\rm pred}\right)^2}{\Delta y_{j,k}^2} & \text{if } N_j^{\rm obs} \leq N_j^{\rm pred} \\ \infty & \text{otherwise} \end{cases} , \quad (4)$$

with the number of image families $N^{\rm fam}$ (in our case 34), the observed and predicted number of multiple images that belong to family j as $N_j^{\rm obs}$ and $N_j^{\rm pred}$, respectively. The observed position of image k from family j is located at $(x_{j,k}^{\rm obs}, y_{j,k}^{\rm obs})$ and matched to the closest model-predicted image position at $(x_{j,k}^{\rm pred}, y_{j,k}^{\rm pred})$, while a predicted image cannot be matched more than once to an observed image. The latter requirement is often neglected and can lead to a lower χ^2 value. Although this definition introduces artificial steep walls in the χ^2 function, we did not find any problems with this simple model rejection. Indeed, it should be possible to find the global minimum, particularly when using simulated annealing starting from high temperatures. In addition, once a parameter set that predicts enough multiple images for all different families was found, the MCMC walkers then explore the parameter space around those parameter values which are expected to lead to models with enough predicted images. In that case, the χ^2 definition reduces to the usual χ^2 function, without steep walls to reject specific models. Another option was recently introduced by Ertl et al. (2024) for the galaxy-scale lensing system HE0230−2130. They checked a posteriori the MCMC chains for the correct image multiplicity. This allowed Ertl et al. (2024) to gain insights into the preferred total mass parametrization of HE0230−2130. We note that this procedure is computationally significantly more expensive, as it also samples models predicting too few multiple images.

We further note that this modified definition still allows more model-predicted images than are included as observables in the model. These additional images could be, for instance, undetected due to a low magnification value, outside of the field of view, or that their exact position has not yet been confirmed. The image position uncertainties are described by $\Delta x_{j,k}$ and $\Delta y_{j,k}$, respectively, in x and y direction. As a consequence, we also modified the usual RMS statistics, and defined it in an analogous way to the expression in Eq. (4), resulting in a RMS value equal

Table 3. Main characteristics of our final cluster mass model in comparison to the model from G16.

Component	Property	Amount	
		G16	This work
Observables	Multiple images	88	106
	families	28	34
	Redshift range	[1.24, 3.70]	[1.24, 5.98]
	cm (spec-z)	164	195
	cm (photo-z)	136	113
Model	cm (fixed)	288	306
	cm (free)	2	2
	DM halos ($q_{\rm H} \neq 1$)	3	3
	DM halos ($q_{\rm H} \equiv 1$)	0	1
	free mass parameters	28	31
	free z parameters	3	3
	d.o.f.	89	110
	RMS	0.26″	0.39″

Notes. Cluster members (cm) are divided into those with Einstein and truncation radii following the scaling relations (fixed) and those outside these relations (free). The fixed cluster members are assumed to be spherical. In the text, we refer to the spherical DM halo as $H_{4\rm N}$.

to or higher than that obtained with the usual definition. With these additional criteria, we were able to build models with the initial parametrization from G16 and correct image multiplicity, but with notably higher χ^2 and RMS values.

Throughout our modeling, we adopted a constant positional uncertainty $\sigma = \Delta x = \Delta y$ that is equal for all images identified in the HFF data, and doubled that value for the images detected only in the MUSE data (i.e., $\sigma = 2 \times \Delta x = 2 \times \Delta y$, see Table 2) as commonly done (e.g., Caminha et al. 2017; Bergamini et al. 2019, 2021). The larger uncertainty associated to the images detected only in MUSE can be ascribed to the lower MUSE spatial resolution and to the possible small offsets relative to the HST images (see Sect. 3.1 for more details on the alignment). This uncertainty, denoted as σ in Fig. 6, was finally adjusted to $\Delta x = \Delta y = 0.32''$, to obtain a χ^2 value similar to the number of degrees of freedom (i.e., to get a reduced χ^2 value of about 1). This rescaling process, prior to sampling the posterior distributions, is crucial to get more realistic statistical uncertainties on the values of the model parameters.

The problem with the image multiplicity and higher χ^2 value indicated that the initial cluster mass model was not flexible enough to reproduce the observed multiple image positions. This is not unexpected, as we included several more families with some of them at significantly higher redshift (e.g., Meneghetti et al. 2017).

With the initial setup, the main contribution to the χ^2 value came from the triple 301 and the quad 401 families (see Fig. 2). Because of this, we tested different possibilities for slightly increasing the model flexibility around the northern galaxy group. In the following, we describe a representative selection of them. For the model selection, we used the Bayesian information criterion (BIC; Schwarz 1978), Akaike information criterion (AIC; Akaike 1974), and AIC with correction for small sample sizes (AICc; Sugiura 1978), under the assumption of the same multiple-image positional uncertainty for all tested models.

First, since the DM halo associated with that specific galaxy group has been neglected so far, we included a fourth PIEMD profile to mimic the DM halo $H_{4\rm N}$, either with a fully free position (i.e., a prior range of $[0'', 60'']$ for both $x_{\rm H}$ and $y_{\rm H}$) or forced to be within the group (through a smaller prior range). In both cases, we only allowed the values of the position and the Einstein radius to vary and required the halo to be spherical. This additional DM halo $H_{4\rm N}$, with only three free parameters, helped significantly to reproduce the image positions of systems 301 and 401.

We further tested the effect of including, instead of $H_{4\rm N}$, two significantly elongated cluster members (marked with filled red circles in Fig. 2) of this group outside of the scaling relations. This means that those two cluster members have free Einstein and truncation radii, as well as a free axis ratio and position angle. Despite the relatively high number of additional free parameters (eight in total), we only achieved a minor improvement. Supported by the BIC, AIC and AICc values, we rejected this variation of the lens mass parametrization.

As an alternative, we exploited the multi-plane (Blandford & Narayan 1986; Schneider et al. 2006) capabilities of GLEE (Suyu & Halkola 2010; Suyu et al. 2012, see e.g., Chirivì et al. 2018; Schuldt et al. 2019; Acebron et al. (in prep.) for detailed application examples) and considered the effect of including, instead of $H_{4\rm N}$, three galaxies that do not belong to the cluster (marked in Fig. 2), but which may significantly affect the lensing potential at their specific redshifts (galaxy 10969 at $z = 0.9759$, galaxy 10875 at $z = 0.2239$, and galaxy 11585 at $z = 0.7495$, see Table A.1). One dPIE profile, with free Einstein and truncation radii, for each of these three galaxies was chosen to represent their total mass contribution. To limit the number of additional free parameters (six in total), we assumed that the profiles are spherical. This also resulted in an improvement compared to the initial parameterization. However, considering the additional free parameters, this is only a minor improvement and not as significant as with $H_{4\rm N}$, which requires only three new parameters.

Moreover, instead of including $H_{4\rm N}$ around the northern galaxy group, we also test the possibility of locating it at the galaxy group position in the north-east, specifically $(-17.0510'', 101.1450'')$ away from the BCG. We fixed the position here but allow the halo to be elliptical, resulting in the same number of additional free parameters (three in total) as for the model with $H_{4\rm N}$ near the multiple image families 301 and 401. However, this configuration is not as good as that with $H_{4\rm N}$. We further considered models containing both $H_{4\rm N}$ and the halo in the north-east, namely, five DM halos in total.

Specifically, we also tried a model that includes the northern halo $H_{4\rm N}$ but with variable axis ratio, position angle, and core radius. In addition, we included the halo located at the north-east with free axis ratio, position angle, and Einstein and core radii, as a fifth DM halo, as well as the two cluster members outside of the scaling relations. This sums up to 15 additional free parameters compared to our final model, resulting in a number of degrees of freedom of 95 instead of 110. With this parameterization, we obtained a RMS value of 0.37″instead of 0.39″. Although this is a notable difference in the achieved RMS value, it does not justify 15 additional parameters based on the BIC, AIC, and AICc values. As a consequence, we finally selected the parametrization with just $H_{4\rm N}$ as our final model, which we discuss in more detail below.

4.5. Results of the final model

Thanks to the additional halo $H_{4\rm N}$ and significant sampling sequences, we were able to achieve a final RMS value of 0.39″, which is notably lower than that with the initial cluster total mass parametrization and the new multiple images. This indicates that the additional halo $H_{4\rm N}$, with only three free parameters,

Table 4. Model parameter estimates, as the median values, with 68% CL (i.e., 1σ) uncertainties and the adopted prior ranges.

Profile	Parameter	Prior	Median $\pm 1\sigma$
1st Halo	$x_{\rm H}$ [″]	$[-60, 60]$	-0.5 ± 0.3
	$y_{\rm H}$ [″]	$[-60, 60]$	$0.40^{+0.21}_{-0.20}$
	$q_{\rm H}$	$[0.2, 1]$	$0.507^{+0.015}_{-0.020}$
	$\phi_{\rm H}$ [rad]	$(-\infty, +\infty)$	0.60 ± 0.02
	$\theta_{\rm E,H}$ [″]	$[0, +\infty)$	$31.5^{+3.1}_{-3.0}$
	$r_{\rm c,H}$ [″]	$[0, +\infty)$	$8.72^{+0.90}_{-0.84}$
2nd Halo	$x_{\rm H}$ [″]	$[-60, 60]$	$-22.6^{+1.6}_{-2.9}$
	$y_{\rm H}$ [″]	$[-60, 60]$	$-26.8^{+1.8}_{-2.9}$
	$q_{\rm H}$	$[0.2, 1]$	$0.67^{+0.11}_{-0.20}$
	$\phi_{\rm H}$ [rad]	$(-\infty, +\infty)$	$0.53^{+0.15}_{-0.35}$
	$\theta_{\rm E,H}$ [″]	$[0, +\infty)$	$8.52^{+1.80}_{-1.65}$
	$r_{\rm c,H}$ [″]	$[0, +\infty)$	7.1 ± 1.8
3rd Halo	$x_{\rm H}$ [″]	$[-60, 60]$	$25.5^{+0.7}_{-1.0}$
	$y_{\rm H}$ [″]	$[-60, 60]$	$47.60^{+0.24}_{-0.25}$
	$q_{\rm H}$	$[0.2, 1]$	$0.217^{+0.030}_{-0.014}$
	$\phi_{\rm H}$ [rad]	$(-\infty, +\infty)$	0.60 ± 0.04
	$\theta_{\rm E,H}$ [″]	$[0, +\infty)$	9.8 ± 0.9
	$r_{\rm c,H}$ [″]	$[0, +\infty)$	$0.93^{+0.40}_{-0.35}$
4th Halo ($H_{\rm 4N}$)	$x_{\rm H}$ [″]	$[0, 60]$	$15.23^{+0.35}_{-0.40}$
	$y_{\rm H}$ [″]	$[0, 60]$	$59.6^{+0.3}_{-0.6}$
	$\theta_{\rm E,H}$ [″]	$[0, +\infty)$	4.5 ± 0.5
Scaling relation	$\theta_{\rm E,BCG}$ [″]	$[0, +\infty)$	1.57 ± 0.24
	$r_{\rm t,BCG}$ [″]	$[0, +\infty)$	$15.8^{+13.0}_{-5.9}$
1st member	q	$[0.2, 1]$	$0.8^{+0.2}_{-0.3}$
	ϕ [rad]	$(-\infty, +\infty)$	$1.45^{+1.05}_{-0.82}$
	$\theta_{\rm E}$ [″]	$[0, +\infty)$	$1.85^{+6.1}_{-0.83}$
	$r_{\rm t}$ [″]	$[0, +\infty)$	$1.04^{+2.45}_{-0.83}$
2nd member	q	$[0.2, 1]$	0.6 ± 0.3
	ϕ [rad]	$(-\infty, +\infty)$	$1.5^{+1.2}_{-1.0}$
	$\theta_{\rm E}$ [″]	$[0, +\infty)$	$2.2^{+4.6}_{-1.1}$
	$r_{\rm t}$ [″]	$[0, +\infty)$	$0.39^{+0.71}_{-0.30}$
photo-z	z_6	$[0, 6]$	$2.76^{+0.20}_{-0.15}$
	z_7	$[0, 6]$	2.74 ± 0.06
	z_8	$[0, 6]$	$2.84^{+0.06}_{-0.05}$

Notes. The positions are given relative to the BCG, Einstein radii are given for a source redshift of infinity, and all position angle values, measured counterclockwise from the positive x-axis, are converted to the range $[0, \pi]$. For the prior ranges, square brackets indicates bounds included in the prior range, while round brackets indicate bounds excluded. The median values and 1σ uncertainties are computed by excluding the first 20 000 accepted iterations as burn-in points.

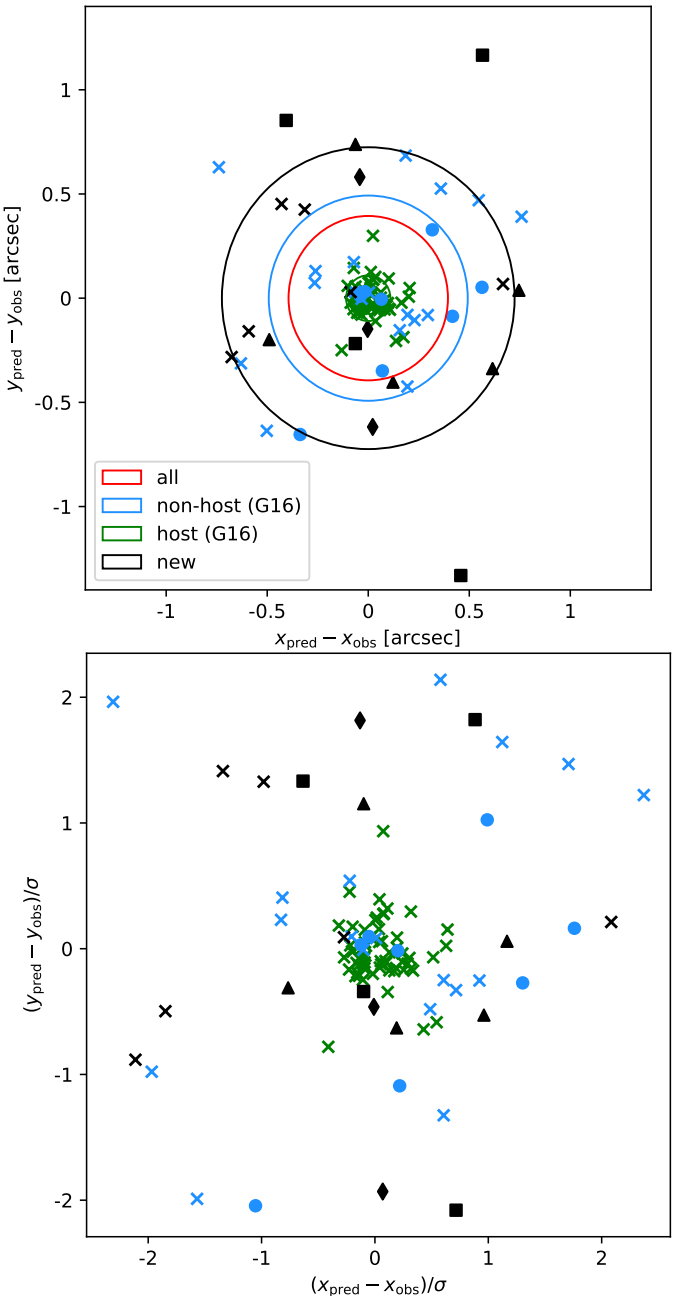

Fig. 6. Separation between predicted and observed image positions of the multiple images (top) and positional differences scaled by the corresponding uncertainty (bottom) for our final reference model. The multiple images are grouped into images (1) belonging to the SN host (green), and at different redshifts, both from (2) G16 (blue) and (3) this work (black) listed in Table 2. We highlight the multiple images with variable redshift (dots), those which are only identified by MUSE (squares for family 401 and triangles otherwise), and family 301 (diamonds). In the top panel, we further indicate the corresponding RMS values and the total RMS of 0.39″ (red) via the radii of the circles.

is amply justified. We provide in Table 3 a summary of the main characteristics of that model, in comparison to the model presented by G16. In Table 4, we list the parameter estimates of the final model, given as the median values with statistical uncertainties defined by the 16th and 84th percentiles (corresponding to the 68% confidence intervals).

Figure 6 shows the contribution to the final RMS of the newly identified multiple images (black) compared to those of the SN host (green) and the non-host images from G16 (blue). In detail, the top panel shows the difference between the model-predicted and observed image positions, with circle radii indicating the corresponding RMS values. This illustrates the significant contribution to the total RMS of the newly identified images, driven mainly by the quad 401 from the northern galaxy group. We recall that this system is only detected in the MUSE datacube, such that we adopt for its images a factor 2 larger position uncertainties $(\Delta x, \Delta y)$, compared to that adopted for the images identified in the HST data. Thus, as shown in the

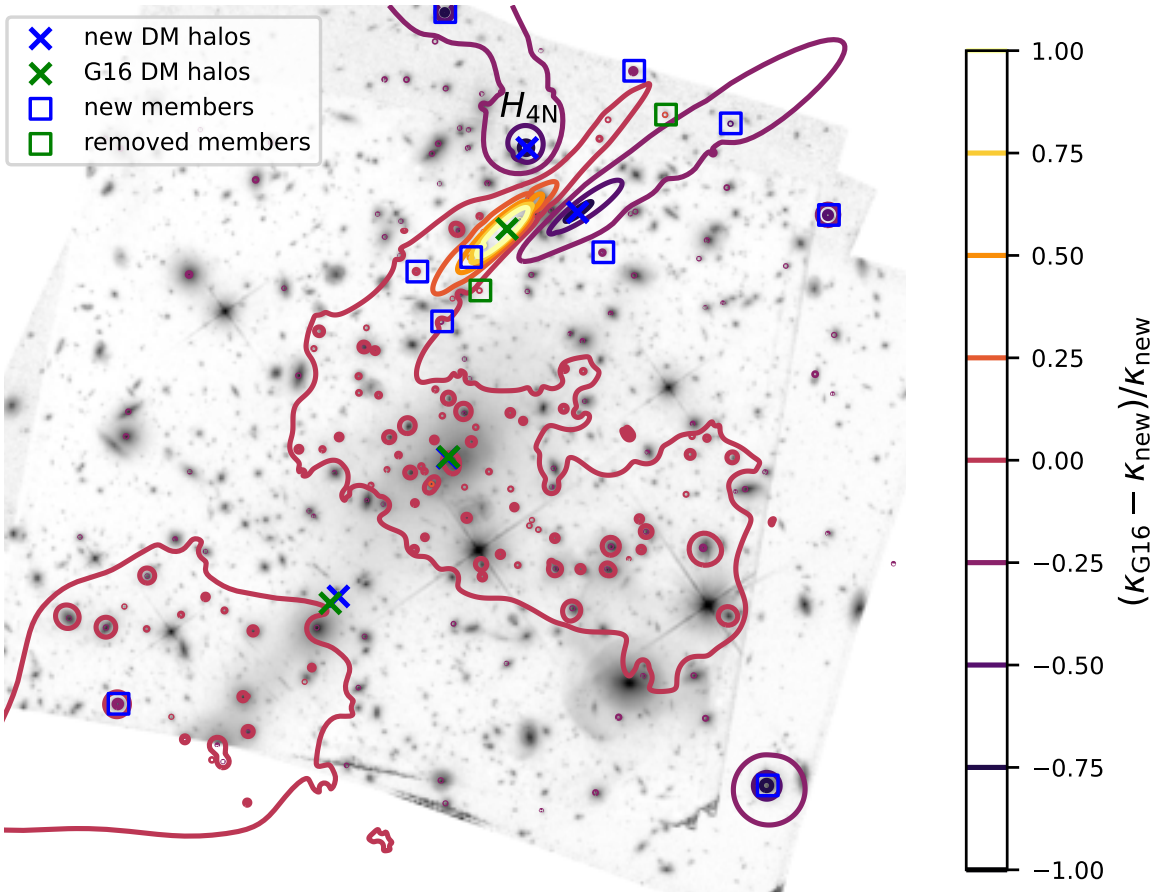

Fig. 7. Relative difference between the convergence map from G16 and our final total mass model, indicated by color-coded contour levels. We highlight the positions of new (blue) and G16/removed mass density profiles (green), for the DM halos (crosses) and cluster members (squares). The spherical halo H_{4N} is also labeled. For an improved orientation, we show in the background the red channel of the HFF color image (see Fig. 1).

bottom panel, the effective contribution of this system to the total χ^2 value, which is the quantity we minimized, is on a similar level compared to other families at different redshifts. We further note that the comparison of the individual χ^2 contribution of each family is difficult, as it depends on the number of their multiple images (e.g., double, triple, quad), on the image distances to the well-constrained regions around the SN Refsdal host images, as well as on their redshift. In addition, three families (IDs 6, 7, and 8; see Table 2 in G16) of the G16 non-host group (blue) are only photometrically confirmed. As noted above, we optimized their redshifts in the range of [0, 6], making it easier to reproduce those image positions. This leads to a lower RMS value for that group of multiple images.

Furthermore, Fig. 6 highlights how well the images of the SN Refsdal host are reproduced, thanks to a large number of different knots (see Table 2 of G16). This implies a good reconstruction of the lens Fermat potential around the multiple images of SN Refsdal, which is crucial for precise and accurate time-delay cosmography, as shown by Grillo et al. (2018, 2020, 2024).

Moreover, we show in Fig. 7 a direct comparison with the best-fitting model of G16, in the form of a κ-map ratio. In detail, we show the ratio of the difference between the κ_{G16} map from G16 and the map from our final model κ_{new}, and κ_{new}, namely, $\frac{\kappa_{G16}(x,y)-\kappa_{new}(x,y)}{\kappa_{new}(x,y)}$.

As expected, the two maps are very similar around the cluster core, where we have most of the observables, while we find larger differences in the north, where we added the additional halo H_{4N} and several new multiple images. We note that the third halo changes its center to compensate for the new mass component. As a reference, we marked the positions of the different halos with a cross, both at the new locations (blue) and the positions published in G16 (green). The positions of the two removed cluster members (green squares) and ten added cluster members (blue squares) are indicated as well, highlighting only minor differences in the κ map. Moreover, the switch from the CLASH to the HFF magnitudes used in the scaling relations explains small deviations at the individual cluster member positions. However, these small differences are expected to have a minor influence on the cluster total mass distribution, which is supported by the well-reproduced image positions of the SN Refsdal host (c. f. Fig. 6).

As a further test, we reconstructed with GLEE the unlensed surface brightness distribution of the SN Refsdal host on a 75×75 pixel grid. This reconstruction is then mapped back to the image plane to obtain the lensed image predicted by the model, which can be directly compared to the observed image. It results in similar residuals, as shown in Fig. 7 of G16 and Fig. 5 of Grillo et al. (2020), which is in agreement with the minor differences in the κ-map reconstruction.

Moreover, we estimated the model-predicted time delays for the multiple images of SN Refsdal and found an agreement well within 1σ compared to the previously predicted values from G16. This demonstrates the robustness of the lensing model around SN Refsdal, thanks to the high number of identified knots of its host galaxy. This comparison is intended as a consistency check of this new model, improved with additional multiple images, but not suited for time-delay cosmography applications. Thus, we refrained from releasing the estimates and refer to future publications for new robust time-delay predictions and cosmological results.

5. Discussion and conclusion

Together with this work, we have released a catalog containing 162 new, secure spectroscopic redshifts obtained from our recent 5h MUSE observations covering a galaxy group north of the lensing cluster MACS 1149. By combining these new redshifts with deep HST images and a re-analysis of the MUSE data cube presented by G16, we identified 17 new and spectroscopically confirmed multiple images, belonging to six different families. This has resulted in 106 secure multiple images from 34 different sources or knots of the SN Refsdal host. It has allowed us to nearly double the number of sources at different redshifts compared to previous publications, and to extend the redshift range by a factor of about 2.

Following previous models of this cluster, we have considered as cluster members in our total mass model all galaxies within the redshift range of $0.52 \leq z \leq 0.57$, down to a magnitude limit of $m_{\rm F160W} \leq 24$. We favored the deep HFF image over the CLASH image used in G16, and released here all measured magnitudes. The new photometric and spectroscopic observations have resulted in the rejection of two previously identified members and the identification of ten new ones, all spectroscopically confirmed by either GLASS (Treu et al. 2016) or MUSE (G16 or this work). Furthermore, with our new redshift catalog, we have confirmed 22 cluster members that had previously only been photometrically selected. In total, we now have 308 secure cluster members, of which 195 (63.3%) have been now spectroscopically confirmed.

The new MUSE observations have allowed us to build an enhanced strong lensing model of MACS 1149. We tested several different total mass parametrizations and obtained our final model, which best reproduces the observed multiple image positions with a limited number of free parameters and a RMS value of $0.39''$. This level of accuracy is well in agreement with similar strong lensing models of various other clusters (e.g., Bergamini et al. 2019, 2021; Caminha et al. 2023). In this final cluster mass model, which is publicly available[4], we have included 308 cluster members each with a dPIE profile. For 306 members, the Einstein and truncation radii are computed through the scaling relations. Moreover, the cluster mass distribution on a larger scale, consisting mainly of the dark matter component of the galaxy cluster and galaxy group, was modeled with four PIEMD profiles, one of which is assumed to be spherical. This has resulted in a total of 34 optimized parameters, along with a χ^2 value of around 110 (for a multiple-image positional uncertainty of $\Delta x = \Delta y = 0.32''$), corresponding to the degrees of freedom of the presented model.

[4] Beside providing the mass density parametrization and the corresponding obtained median values in Table 4, we release the model at the following link upon publication: https://www.fe.infn.it/astro/lensing/

While exploiting and presenting extensive spectroscopic data from MUSE and imaging data from HST, this cluster has been recently observed by the JWST (PIs N. Luetzgendorf, M. Stiavelli, F. Sun, C. Willott) to complement the existing data of this unique lens. These observations will reveal details of several high redshift sources, including the object called JD1 (Hashimoto et al. 2018) located in the north-west of MACS 1149 at a redshift of $z = 9.1$, as presented by Hashimoto et al. (2018) and Stiavelli et al. (2023). Although we have extended our total mass model further to the north with the presented MUSE observations, the model still lacks constraints in the region around JD1. Further details of this extreme and peculiar source – or sources – (see Fig. 1 of Stiavelli et al. 2023) are required to better understand its physical properties.

The JWST NIRSpec and NIRCam observations will allow us to reveal and spectroscopically confirm additional multiply lensed sources and to identify more knots in known multiple images. With our presently improved total mass model of MACS 1149, we have paved the way to incorporating these JWST data. Moreover, while this model is optimized using the observed multiple image positions only, it will enable us to build an extended strong lensing model that exploits the deep HST (and JWST) images through the reconstruction of the surface brightness distribution of the SN Refsdal host galaxy. This will increase the number of observables around the multiple images of SN Refsdal by around two orders of magnitude and offer the unique opportunity to demonstrate and visualize the accuracy of the cluster total mass model. This will also be crucial to improving the cosmographic measurements (see e.g., Grillo et al. 2024) with the time delays of supernovae strongly lensed by galaxy clusters.

Acknowledgements. We thank Ana Acebron and the anonymous referee for helpful discussions and comments. We acknowledge financial support through grants PRIN-MIUR 2017WSCC32 and 2020SKSTHZ. SS has received funding from the European Union's Horizon 2022 research and innovation programme under the Marie Skłodowska-Curie grant agreement No 101105167 - FASTIDIoUS. AM acknowledges financial support through grant NextGenerationEU" RFF M4C2 1.1 PRIN 2022 project 2022ZSL4BL INSIGHT. SHS thanks the Max Planck Society for support through the Max Planck Fellowship. This project has received funding from the European Research Council (ERC) under the European Union's Horizon 2020 research and innovation programme (LENSNOVA: grant agreement No 771776). This research is supported in part by the Excellence Cluster ORIGINS which is funded by the Deutsche Forschungsgemeinschaft (DFG, German Research Foundation) under Germany's Excellence Strategy – EXC-2094 – 390783311. This research is based on observations made with the NASA/ESA *Hubble* Space Telescope obtained from the Space Telescope Science Institute, which is operated by the Association of Universities for Research in Astronomy, Inc., under NASA contract NAS 5-26555. Based on observations collected at the European Southern Observatory under ESO programmes 294.A-5032 and 105.20P5.001. Software Citations: This work uses the following software packages: `Astropy` (Astropy Collaboration 2013, 2018), `Emcee` (Foreman-Mackey et al. 2013), `matplotlib` (Hunter 2007), `NumPy` (van der Walt et al. 2011; Harris et al. 2020), `Python` (Van Rossum & Drake 2009), `Scipy` (Virtanen et al. 2020).

References

Akaike, H. 1974, IEEE Trans. Autom. Control, 19, 716
Annunziatella, M., Mercurio, A., Biviano, A., et al. 2016, A&A, 585, A160
Astropy Collaboration (Robitaille, T. P., et al.) 2013, A&A, 558, A33
Astropy Collaboration (Price-Whelan, A. M., et al.) 2018, AJ, 156, 123
Bacon, R., Accardo, M., Adjali, L., et al. 2012, The Messenger, 147, 4
Bergamini, P., Rosati, P., Mercurio, A., et al. 2019, A&A, 631, A130
Bergamini, P., Rosati, P., Vanzella, E., et al. 2021, A&A, 645, A140
Bergamini, P., Acebron, A., Grillo, C., et al. 2023, ApJ, 952, 84
Blandford, R., & Narayan, R. 1986, ApJ, 310, 568
Calura, F., Vanzella, E., Carniani, S., et al. 2021, MNRAS, 500, 3083
Caminha, G. B., Grillo, C., Rosati, P., et al. 2017, A&A, 600, A90

Caminha, G. B., Grillo, C., Rosati, P., et al. 2023, A&A, 678, A3
Cerny, C., Sharon, K., Andrade-Santos, F., et al. 2018, ApJ, 859, 159
Chirivì, G., Suyu, S. H., Grillo, C., et al. 2018, A&A, 614, A8
Coe, D., Zitrin, A., Carrasco, M., et al. 2013, ApJ, 762, 32
Elíasdóttir, Á., Limousin, M., Richard, J., et al. 2007, ArXiv e-prints [arXiv:0710.5636]
Ertl, S., Schuldt, S., Suyu, S. H., et al. 2023, A&A, 672, A2
Ertl, S., Schuldt, S., Suyu, S. H., et al. 2024, A&A, 685, A15
Foreman-Mackey, D., Hogg, D. W., Lang, D., & Goodman, J. 2013, PASP, 125, 306
Frye, B. L., Pascale, M., Pierel, J., et al. 2024, ApJ, 961, 171
Fukugita, M., Ichikawa, T., Gunn, J. E., et al. 1996, AJ, 111, 1748
Golovich, N., Dawson, W. A., Wittman, D., et al. 2016, ApJ, 831, 110
Grillo, C., Suyu, S. H., Rosati, P., et al. 2015, ApJ, 800, 38
Grillo, C., Karman, W., Suyu, S. H., et al. 2016, ApJ, 822, 78
Grillo, C., Rosati, P., Suyu, S. H., et al. 2018, ApJ, 860, 94
Grillo, C., Rosati, P., Suyu, S. H., et al. 2020, ApJ, 898, 87
Grillo, C., Pagano, L., Rosati, P., & Suyu, S. H. 2024, A&A, 684, L23
Harris, C. R., Millman, K. J., van der Walt, S. J., et al. 2020, Nature, 585, 357
Hashimoto, T., Laporte, N., Mawatari, K., et al. 2018, Nature, 557, 392
Hunter, J. D. 2007, Comput. Sci. Eng., 9, 90
Jouvel, S., Host, O., Lahav, O., et al. 2014, A&A, 562, A86
Karman, W., Grillo, C., Balestra, I., et al. 2016, A&A, 585, A27
Kassiola, A., & Kovner, I. 1993, ApJ, 417, 450
Kelly, P. 2016, IAU Focus Meeting, 29B, 822
Kelly, P. L., Rodney, S. A., Brammer, G., et al. 2015a, ATel, 8402, 1
Kelly, P. L., Rodney, S. A., Treu, T., et al. 2015b, Science, 347, 1123
Kelly, P. L., Rodney, S. A., Treu, T., et al. 2016, ApJ, 819, L8
Kelly, P. L., Rodney, S., Treu, T., et al. 2023, ApJ, 948, 93
Koekemoer, A. M., Aussel, H., Calzetti, D., et al. 2007, ApJS, 172, 196
Koekemoer, A. M., Faber, S. M., Ferguson, H. C., et al. 2011, ApJS, 197, 36
Limousin, M., Richard, J., Jullo, E., et al. 2016, A&A, 588, A99
Meneghetti, M., Natarajan, P., Coe, D., et al. 2017, MNRAS, 472, 3177
Meneghetti, M., Davoli, G., Bergamini, P., et al. 2020, Science, 369, 1347
Meneghetti, M., Ragagnin, A., Borgani, S., et al. 2022, A&A, 668, A188
Meneghetti, M., Cui, W., Rasia, E., et al. 2023, A&A, 678, L2
Mercurio, A., Rosati, P., Biviano, A., et al. 2021, A&A, 656, A147
Meštrić, U., Vanzella, E., Zanella, A., et al. 2022, MNRAS, 516, 3532
Morishita, T., Stiavelli, M., Grillo, C., et al. 2024a, ApJ, 971, 43
Morishita, T., Stiavelli, M., Schuldt, S., & Grillo, C. 2024b, ApJ, submitted [arXiv:2404.10037]
Ogrean, G. A., van Weeren, R. J., Jones, C., et al. 2016, ApJ, 819, 113
Oke, J. B., & Gunn, J. E. 1983, ApJ, 266, 713
Peng, C. Y., Ho, L. C., Impey, C. D., & Rix, H.-W. 2002, AJ, 124, 266
Pierel, J. D. R., Newman, A. B., Dhawan, S., et al. 2024, ApJ, 967, L37
Postman, M., Coe, D., Benítez, N., et al. 2012, ApJS, 199, 25
Raney, C. A., Keeton, C. R., & Zimmerman, D. T. 2021, MNRAS, 508, 5587
Rau, S., Vegetti, S., & White, S. D. M. 2014, MNRAS, 443, 957
Rodney, S. A., Strolger, L. G., Kelly, P. L., et al. 2016, ApJ, 820, 50
Rodney, S. A., Brammer, G. B., Pierel, J. D. R., et al. 2021, Nat, Astron., 5, 1118
Schmidt, K. B., Treu, T., Brammer, G. B., et al. 2014, ApJ, 782, L36
Schneider, P., Kochanek, C., & Wambsganss, J. 2006, Gravitational Lensing: Strong, Weak and Micro - Saas-Fee Advanced Course 33 (Berlin Heidelberg: Springer Science & Business Media)
Schuldt, S., Chirivì, G., Suyu, S. H., et al. 2019, A&A, 631, A40
Schuldt, S., Suyu, S. H., Cañameras, R., et al. 2023, A&A, 673, A33
Schwarz, G. 1978, Ann. Stat., 6, 461
Shajib, A. J., Treu, T., Birrer, S., & Sonnenfeld, A. 2021, MNRAS, 503, 2380
Shajib, A. J., Wong, K. C., Birrer, S., et al. 2022, A&A, 667, A123
Smith, G. P., Ebeling, H., Limousin, M., et al. 2009, ApJ, 707, L163
Stiavelli, M., Morishita, T., Chiaberge, M., et al. 2023, ApJ, 957, L18
Sugiura, N. 1978, Commun. Stat. Theory. Methods, 7, 13
Suyu, S. H., & Halkola, A. 2010, A&A, 524, A94
Suyu, S. H., Hensel, S. W., McKean, J. P., et al. 2012, ApJ, 750, 10
Suyu, S. H., Goobar, A., Collett, T., More, A., & Vernardos, G. 2024, Space Sci. Rev., 220, 13
Treu, T., & Ellis, R. S. 2015, Contemp. Phys., 56, 17
Treu, T., Brammer, G., Diego, J. M., et al. 2016, ApJ, 817, 60
Treu, T., Suyu, S. H., & Marshall, P. J. 2022, A&A Rev., 30, 8
van der Walt, S., Colbert, S. C., & Varoquaux, G. 2011, Comput. Sci. Eng., 13, 22
Van Rossum, G., & Drake, F. L. 2009, Python 3 Reference Manual (Scotts Valley, CA: CreateSpace)
Vanzella, E., Caminha, G. B., Rosati, P., et al. 2021, A&A, 646, A57
Virtanen, P., Gommers, R., Oliphant, T. E., et al. 2020, Nat. Methods, 17, 261
Wang, H., Cañameras, R., Caminha, G. B., et al. 2022, A&A, 668, A162
Wong, K. C., Suyu, S. H., Chen, G. C. F., et al. 2020, MNRAS, 498, 1420
Zheng, W., Postman, M., Zitrin, A., et al. 2012, Nature, 489, 406

Appendix A: MUSE redshift catalog

We release in Table A.1 the full MUSE redshift catalog (see Sect. 3 for details on the data reduction and redshift extraction). We divide into foreground, cluster members, and background objects. This catalog is also online[4] available together with our strong lensing model quantities.

Table A.1. MUSE catalog from new pointing.

ID	R.A. (J2000)	Decl. (J2000)	z_{sp}	QF
1934	177.386230	22.402407	0.0000	3
10773	177.385284	22.415760	0.0000	3
11827	177.395355	22.410061	0.0000	3
175	177.402374	22.407394	0.0000	3
10875	177.392548	22.412317	0.2239	3
11239	177.391602	22.413786	0.2405	9
12173	177.386124	22.408899	0.2658	9
11010	177.386307	22.416983	0.3707	3
13059	177.397049	22.404455	0.4246	3
11899	177.400131	22.410467	0.4300	3
12148	177.392380	22.409252	0.4392	3
12927	177.389771	22.405228	0.4945	3
13125	177.395447	22.404039	0.5139	3
13578	177.392883	22.403997	0.5142	3
77	177.386322	22.403538	0.5262	2
7566	177.390961	22.401681	0.5274	3
10943	177.383530	22.414936	0.5277	3
10872	177.394714	22.411367	0.5282	3
10749	177.382568	22.416515	0.5290	3
10825	177.392563	22.410583	0.5303	3
11562	177.388306	22.411697	0.5303	3
11205	177.386620	22.413649	0.5311	3
13285	177.391037	22.403284	0.5323	2
11547	177.401596	22.411303	0.5336	3
12244	177.400696	22.408604	0.5337	2
12955	177.403061	22.404383	0.5339	3
250	177.390732	22.409433	0.5340	2
11888	177.393356	22.410439	0.5341	3
10466	177.391098	22.404907	0.5343	3
10542	177.391830	22.405287	0.5343	3
11038	177.394730	22.414410	0.5347	3
11202	177.386383	22.413706	0.5352	3
12411	177.391342	22.407789	0.5360	3
10412	177.398193	22.416279	0.5362	3
11009	177.388107	22.413761	0.5372	3
11922	177.396805	22.410011	0.5379	3
13521	177.393814	22.402306	0.5381	3
12783	177.398453	22.405361	0.5382	3
11974	177.383591	22.410727	0.5382	3
10838	177.397720	22.415215	0.5388	3
11951	177.394073	22.412720	0.5391	3
10492	177.383721	22.417095	0.5395	3
11618	177.397034	22.411560	0.5406	3
12791	177.399261	22.405941	0.5418	3
11559	177.388031	22.411810	0.5418	3
12377	177.394043	22.408434	0.5421	3
13256	177.392105	22.403413	0.5423	2
10787	177.390106	22.415707	0.5423	3
12629	177.384003	22.406673	0.5429	3
13006	177.397980	22.404575	0.5433	2
13114	177.390152	22.403889	0.5443	3
11346	177.392942	22.411877	0.5445	3
11468	177.399490	22.412281	0.5471	2
10891	177.382751	22.413095	0.5474	3
12443	177.394272	22.407550	0.5474	3
12242	177.398163	22.407408	0.5475	3
10247	177.403717	22.404572	0.5476	3
10743	177.383163	22.415918	0.5478	3
12261	177.401642	22.409443	0.5480	2
13133	177.397919	22.403936	0.5486	3
11722	177.387070	22.411036	0.5495	3
10946	177.395233	22.414932	0.5501	3
10766	177.398132	22.415958	0.5506	2
10688	177.398300	22.416018	0.5518	2
10865	177.384674	22.414953	0.5518	2
12169	177.388123	22.408403	0.5529	3
12900	177.389465	22.406374	0.5531	3
11759	177.383896	22.410284	0.5537	3
11162	177.390289	22.413977	0.5540	2
10236	177.395798	22.418215	0.5542	2
10846	177.399804	22.414903	0.5546	3
10217	177.396835	22.417459	0.5550	3
12379	177.384369	22.409304	0.5550	3
10239	177.396912	22.418097	0.5553	3
10233	177.392883	22.418200	0.5561	3
11341	177.393127	22.411263	0.5567	3
10760	177.397675	22.416185	0.5571	3
10144	177.399002	22.418392	0.5576	3
139	177.403580	22.405603	0.5582	2
284	177.396820	22.410732	0.5584	2
10888	177.399429	22.415444	0.5589	3
12099	177.389938	22.409636	0.5592	3
12096	177.397568	22.409370	0.5606	2
11151	177.396591	22.413328	0.5607	3
11372	177.393830	22.411690	0.5608	3
11297	177.399353	22.413298	0.5609	3
10993	177.392181	22.414761	0.5612	3
11289	177.394211	22.412466	0.5620	3
11671	177.398270	22.410788	0.5645	3
10	177.389145	22.401512	0.5656	9
11033	177.388870	22.414148	0.5666	3
12499	177.397049	22.407593	0.5667	3
245	177.401636	22.409258	0.741	3
10845	177.384064	22.413107	0.742	3
11585	177.393600	22.410720	0.750	3
10564	177.393753	22.417341	0.821	3
10579	177.398300	22.419676	0.838	3
10606	177.382324	22.415525	0.849	3
12318	177.402664	22.408005	0.851	3
10789	177.395264	22.417244	0.863	3
11551	177.386093	22.411703	0.863	3
11023	177.382584	22.414490	0.886	3
12845	177.401650	22.405742	0.962	3
10969	177.393440	22.412600	0.976	3
243	177.386627	22.409378	0.979	3
45	177.387207	22.402948	1.026	3
10341	177.401001	22.404701	1.086	3
9681	177.397049	22.421038	1.089	9
12906	177.398499	22.405746	1.089	3

Table A.1. continued.

ID	R.A. (J2000)	Decl. (J2000)	z_{sp}	QF
10678	177.395538	22.416037	1.103	3
11122	177.385842	22.413897	1.274	3
11107	177.385986	22.414076	1.274	3
12028	177.383514	22.410889	1.276	3
10679	177.381729	22.416651	1.377	3
10093	177.391976	22.419028	1.482	9
13021	177.400391	22.406767	1.600	3
12760	177.397018	22.406183	1.678	3
12761	177.397217	22.406183	1.678	3
10972	177.392929	22.415367	1.806	2
10942	177.393921	22.413961	2.347	3
10584	177.394073	22.416553	2.488	3
11775	177.383316	22.409315	2.768	3
13088	177.387924	22.404253	2.771	2
13019	177.387222	22.404619	3.017	3
2153	177.392426	22.402571	3.130	2
12424	177.401169	22.407183	3.130	3
22820	177.392715	22.403093	3.131	3
13293	177.392786	22.403189	3.131	3
2191	177.393021	22.403545	3.132	3
562	177.383587	22.409872	3.188	3
560	177.384083	22.410684	3.188	3
561	177.383709	22.410443	3.188	3
563	177.384075	22.410203	3.188	3
12338	177.401703	22.408350	3.188	3
10816	177.388123	22.415678	3.215	3
210	177.386322	22.408720	3.219	9
564	177.391847	22.417813	3.388	9
301.1	177.395027	22.412690	3.447	9
301.2	177.393511	22.413066	3.447	3
301.3	177.392831	22.412863	3.447	3
550	177.391884	22.408651	3.483	2
549	177.391557	22.408464	3.483	3
565	177.383499	22.414271	3.531	9
3019	177.398224	22.414471	3.532	9
10098	177.396378	22.419118	3.574	3
566	177.389469	22.418364	3.597	9
13261	177.391678	22.403515	3.704	3
13457	177.390839	22.402636	3.705	3
567	177.386664	22.417851	3.824	3
546	177.395420	22.415347	4.161	3
202.1	177.400121	22.404141	4.384	3
202.2	177.398323	22.403761	4.384	3
12420	177.384079	22.408073	4.734	3
568	177.397473	22.411118	4.845	3
22804	177.388626	22.402992	5.033	9
204.1	177.400379	22.403885	5.806	9
204.2	177.399437	22.403754	5.806	9
401.1	177.391676	22.411496	5.983	9
401.2	177.395838	22.412362	5.983	3
401.3	177.393575	22.411423	5.983	3
401.4	177.393185	22.413001	5.983	9
2364	177.387711	22.405834	6.155	9

Notes. Columns give, from left to right, the identification number ID, right ascension, declination, spectroscopic redshift z_{sp}, and the corresponding uncertainty in terms of a quality flag QF, with 3 as very secure ($\delta z < 0.001$), 2 as secure ($\delta z < 0.01$), and 9 as secure (based on a single emission line).